arXiv:1304.2589v1 [nucl-ex] 9 Apr 2013

High-statistics measurement of the β-delayed α spectrum of ^{20}Na

K. L. Laursen,[1, *] O. S. Kirsebom,[1, 2] H. O. U. Fynbo,[1] A. Jokinen,[3]
M. Madurga,[4, †] K. Riisager,[1] A. Saastamoinen,[3, ‡] O. Tengblad,[4] and J. Äystö[3, 5]

[1] *Department of Physics and Astronomy, Aarhus University, DK-8000 Aarhus C, Denmark*
[2] *TRIUMF, Vancouver, British Columbia, V6T 2A3, Canada*
[3] *Department of Physics, University of Jyväskylä, FIN-40351 Jyväskylä, Finland*
[4] *Instituto de Estructura de la Materia, CSIC, Serrano 113 bis, E-28006 Madrid, Spain*
[5] *Helsinki Institute of Physics, FI-00014 University of Helsinki, Finland*

A measurement of the ^{20}Na β-delayed alpha spectrum with a high-granularity set-up has allowed the decay scheme to be revised on several points. Three new transitions of low intensity are found at low α-particle energy. An R-matrix fit of the complete spectrum gives an improved description of the decay and indicates feeding to the broad 2^+ α-cluster state close to 9 MeV.

PACS numbers: 23.40.–s, 27.30.–t, 29.30.Ep, 21.10.Hw

I. INTRODUCTION

The $J^\pi = 2^+$, $T = 1$ ground state of ^{20}Na decays to ^{20}Ne by positron emission with a half-life of 447.9(23) ms and an available decay energy of $Q_{\rm EC} = 13\,892.5(11)$ keV [1]. Excited states in ^{20}Ne populated in the β decay of ^{20}Na, with an excitation energy above 4 729.84 keV, may break up to $\alpha + {}^{16}$O. The α particles originating from such transitions are referred to as β-delayed α particles and have been the subject of numerous experimental investigations.

Through angular correlation studies, see e.g. Refs. [2, 3], the ratio of the Fermi (vector) and the Gamow-Teller (axial-vector) component has been determined for a number of allowed transitions including the $J^\pi = 2^+$, $T = 1$ isobaric analog state (IAS) at 10 273 keV. For several transitions to $J^\pi = 2^+$, $T = 0$ states in ^{20}Ne, limits have been set on the Fermi contribution and from this the ^{20}Ne isospin mixing has also been established.

Through measurements of ft values to individual levels in ^{20}Ne and comparison to the ft values in the mirror decay, $^{20}\text{F} \rightarrow {}^{20}\text{Ne}^* + \beta^+ + \nu_e$, the energy-dependence of the mirror asymmetry has been studied, yielding information on nuclear structure, meson exchange currents, and second-class currents, see e.g. Refs. [3, 4].

The data presented here were originally intended as calibration data for a precision measurement of the β decay of ^{8}B [5], but the quality and high statistics of the data reveals new features of the decay scheme of ^{20}Na. New transitions appear at low α particle energies and clear signatures of interference leads to a reinterpretation of the decay scheme at higher α-particle energies. In particular, we shall present evidence for the population of a broad resonance in ^{20}Ne, indicative of a $\alpha + {}^{16}$O cluster structure. It can be studied in a very clean way through β decay since the initial state and the transition operator are well understood so that the final state is the only unknown, see Ref. [6] for a similar study in the $A = 12$ system.

The broad (cluster) states can play a role in the $^{16}\text{O}(\alpha,\gamma)^{20}$Ne reaction, which proceeds at a slow rate during astrophysical He burning due to the absence of natural-parity resonances inside the Gamow window. Recently Hager *et al.* [7] measured the total S-factor at $E_{\rm c.m.} = 2.26$ MeV and determined the contributions from direct capture transitions to the ground and first-excited state. Costantini *et al.* [8] determined S-factor values for a range of energies and used an R-matrix fit to extrapolate the S-factor down to the energies relevant for astrophysics, but they left out the broad 0^+ and 2^+ resonances of the fourth 0^+ rotational band of ^{20}Ne. Our results may allow to judge more precisely the effect on the S-factor of the low-energy tail of the 2^+_4 resonance.

II. EXPERIMENT

A. Beam production

The radioactive ^{20}Na beam was produced at the Accelerator Laboratory of University of Jyväskylä through the $^{24}\text{Mg}(p, n\alpha)^{20}$Na reaction. The proton primary beam had an energy of 40 MeV and a typical intensity of 8 − 10 μA, and the target was self-supporting 4.3 mg/cm^2 natural Mg. The activity was extracted with the Ion Guide Isotope Separation On-Line (IGISOL) technique [9], using a light-ion fusion ion guide [10] and the mass separated $A/q = 20$ beam was implanted in a carbon foil of thickness 26 ± 2 μg/cm^2. The acceleration voltage was 20 kV resulting in the ions, on average, being implanted at a depth of 7.4 μg/cm^2. The average ^{20}Na implantation rate was 2.2×10^4 ions per second.

Data taking was split in two runs, the first lasting 5 hours, the second 7 hours. In between, the setup was used for measuring the decays of ^{23}Al (8 hours) and ^{8}B

---

[*] Corresponding author: klj06@phys.au.dk
[†] Present address: Physics Division, Oak Ridge National Laboratory, Oak Ridge, TN 37831, USA.
[‡] Present address: Cyclotron Institute, Texas A&M University, College Station, TX 77843-3366, USA

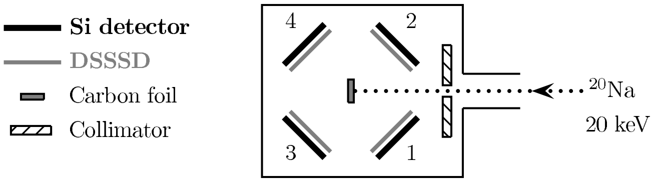

FIG. 1: Schematic and simplified illustration of the experimental setup (top view).

(72 hours). At no point during this interval was the vacuum broken. The ^{8}B and ^{23}Al measurements are discussed elsewhere [5, 11]. The two ^{20}Na runs give consistent results.

B. Detection system

The set-up consisted of four 60 μm thick, double sided silicon strip detectors (DSSSD) [12] backed by 1.5 mm thick, unsegmented silicon detectors used to veto against β particles. The detectors were placed 5 cm from the carbon foil in a rectangular configuration with the carbon foil perpendicular to the beam, see Fig. 1. The total solid-angle coverage was 30% and the angular resolution 3 degrees. An important feature of the DSSSDs is the very thin dead layer of only 100 nm (over 95 - 96% of the active surface) which facilitates the detection of low-energy ions [12]. The energy resolution of the DSSSDs was 25 keV (FWHM).

The trigger thresholds of the data acquisition system were set as low as possible above the noise and were studied with an ^{241}Am source in air at atmospheric pressure [5]. The trigger efficiency was found to rise gently as a function of energy, increasing from 0% to 100% within an interval of roughly 100 keV. The trigger thresholds, defined as the energy at which the efficiency reaches 50%, ranged from 160 to 240 keV, depending on the electronics channel. Low-energy particles below the trigger threshold could be detected if in coincidence with a higher-energy particle. Low-energy cutoffs in each ADC channel ranged from 60 to 230 keV.

C. Energy calibration

The two most intense β-delayed α lines of ^{20}Na at 2153.2(10) keV and 4433.8(15) keV were used for the energy calibration. Their energies were deduced from the excitation energies, 7421.9(12) keV and 10273.2(19) keV, of the corresponding states in ^{20}Ne and the $\alpha + {}^{16}$O threshold energy of 4729.84(1) keV given in Ref. [13]. SRIM stopping power tables [14] were used to correct for the energy loss of the α particles and the ^{16}O ions in the carbon foil and the detector dead layer, taking into account the variation in effective thickness with angle, but assuming a fixed implantation depth in the foil. Corrections were also made for the non-ionizing energy loss in the active volume of the detector which does not contribute to the observed signal. The calibration includes a 5 keV quadratic component due to a non-linearity in the electronical response (deduced from measurements with a precision pulse generator) and a 20 keV quadratic component due to the changing pulse shape of physical particles at low energies. See Ref. [5] for further details.

III. DATA ANALYSIS AND RESULTS

The singles- and coincidence α-spectra, summed over all four detectors, obtained in the second run are shown in Fig. 2. The ^{16}O recoil lines corresponding to the two most intense α lines (5 and 9) are clearly visible in the singles spectrum at 540 and 1 110 keV, i.e. one-fourth of the α-particle energies. Only coincidence events which fulfill the requirement $E_{^{16}\mathrm{O}} < \frac{1}{4}E_{\alpha} + 75$ keV are used to generate the coincidence spectrum. This cut greatly reduces the response tails. In particular, the response tail of the most intense α line (5) is greatly reduced, clearly exposing the new α lines below 1.5 MeV. Satellite peaks, caused by additional energy loss of α particles striking the aluminum grid covering 4–5% of the detector surface, are visible on the low-energy flank of the two most intense α lines and are marked with asterisks.

A. New low-energy lines

This section is concerned with α lines 1–4; lines 1–3 have not been observed previously. As we shall argue, lines 1 and 2 may be identified with α decays of the 3^{-}, $T = 0$ state at 5 621.4(17) keV and the 1^{-}, $T = 0$ state at 5 787.7(26) keV. The corresponding α-particle energies are 713 keV and 846 keV and the ^{16}O energies are 178 keV and 212 keV. The two new α lines are only seen in DSSSD 3, the reason being that DSSSD 2, which is placed opposite of DSSSD 3, is the only detector with sufficiently low ADC cutoffs to detect the coincident ^{16}O ions. The ^{16}O ions lose a substantial part of their energy in the carbon foil and in the detector dead layer. At average implantation depth and 45° exit angle, the energy loss is approximately 50 keV. In the active volume of the detector another 30 keV is lost to non-ionizing processes, thus reducing the detectable ^{16}O energies to approximately 100 and 130 keV, respectively, which is comparable to the typical ADC cutoff in DSSSD 2. Below, we discuss the consequences this has for the low-energy α lines.

1. *Reduced detection efficiency and energy shift*

The implantation-depth distribution of 20 keV ^{20}Na ions in carbon obtained from a TRIM simulation [14] is shown by the solid line in Fig. 3. The large width of

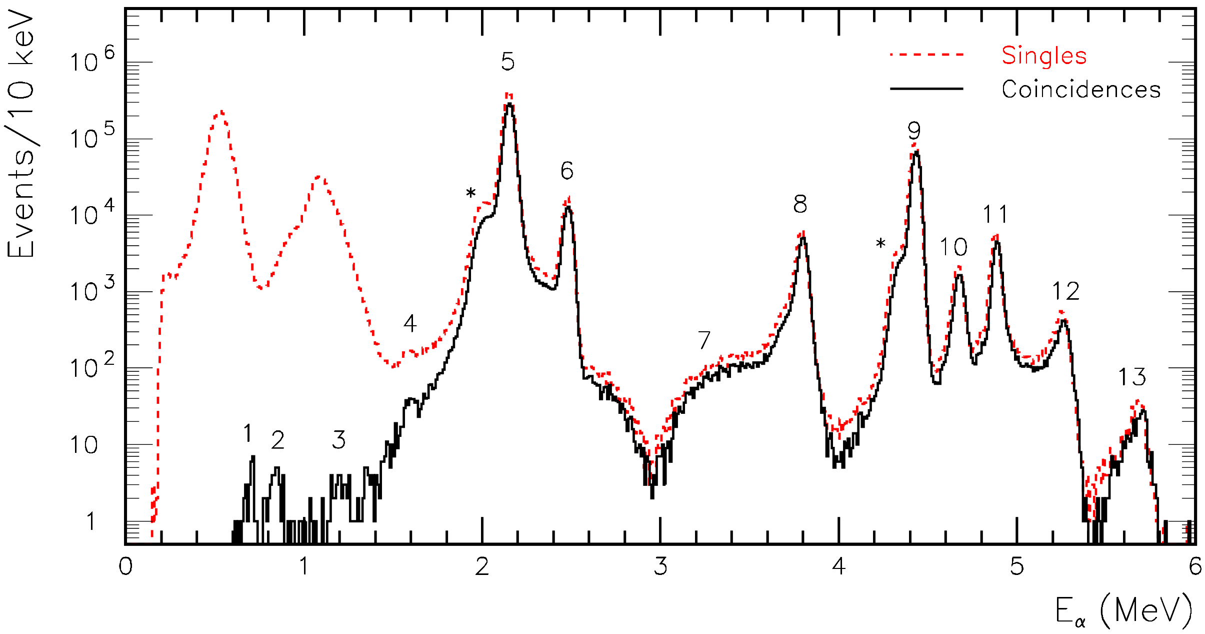

FIG. 2: (Color online) β-delayed α spectrum of ^{20}Na. The solid line (black) is the $\alpha + {}^{16}$O coincidence spectrum. The dashed line (red) is the singles spectrum. The ^{16}O recoil lines visible at 540 and 1 110 keV, corresponds to the two most intense α lines (5 and 9). Asterisks indicate satellite peaks due to the additional energy lost by α particles striking the detector aluminum grid.

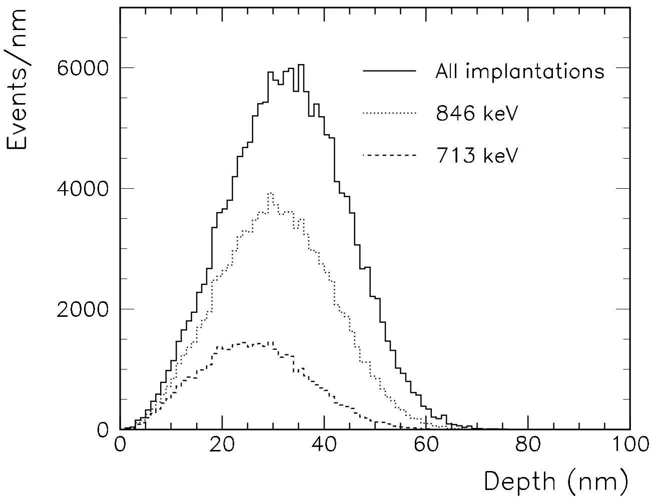

FIG. 3: Implantation-depth distributions obtained from Monte Carlo simulations showing the reduction in coincidence-detection efficiency and the apparent shift toward shallow implantation for the α lines at 713 keV and 846 keV.

the distribution causes a significant broadening of the ^{16}O energies ($\approx$ 30 keV FWHM), with shallow implantations giving the largest ^{16}O energies because DSSSD 2 is located upstream with respect to the foil. The recoil shift discussed in Section III C 2 also contributes to the broadening ($\approx$ 30 keV FWHM). Owing to the ADC cutoffs there exists a preference for shallow implantation and positive recoil shift, implying a larger-than-average energy loss and a negative recoil shift for the α particles.

To determine the reduction in coincidence-detection efficiency and the shift in the apparent α-particle energy due to the effects discussed above, we perform Monte Carlo simulations [5]. The reduction in detection efficiency and the preference for shallow implantation is clearly seen in Fig. 3, which shows implantation-depth distributions predicted by the Monte Carlo simulations: If all implantations are considered, the solid distribution results. If, on the other hand, we only consider implantations where both the α particle and the ^{16}O ion are detected, the dotted and the dashed distributions result.

In the first run, α lines 1 and 2 are observed at 699(4) keV and 849(8) keV. The apparent shift in α energy determined from the simulations are $-14(5)$ keV and $-4(4)$ keV. The systematic uncertainty on the energy shifts was estimated by performing simulations with all ADC cutoffs raised and lowered by 10 keV and with the detector dead layer increased and decreased by 10%. Correcting the observed energies for the shifts, we obtain 713(6) keV and 853(9) keV. In the second run, α lines 1 and 2 are observed at 698(4) keV and 838(5) keV. The α energy shifts determined from the simulations are $-16(5)$ keV and $-6(4)$ keV. Compared to the first run, the shifts in α energy are slightly larger. This is due to the accumulation of material on the foil between the two runs, resulting in a 20% increase in foil thickness. Correcting the observed energies for the bias, we obtain 714(6) keV and 844(9) keV. Taking the average of the

TABLE I: Relative intensities of α lines 1–5 and 9. N is the number of coincidence events observed in the first (top) and second (bottom) run with the α particle detected in DSSSD 3 and the ^{16}O ion detected in DSSSD 2. ε is the coincidence-detection efficiency determined from Monte Carlo simulations (arbitrarily fixed to 100% for line 9). I is the efficiency-corrected intensity relative to that of line 5 with the statistical uncertainties given in parentheses. The average of the two runs is given in the next-to-last column and the systematic uncertainty on the intensity is given in the last column.

Line	N	ε (%)	I (%)		Syst. uncert.
1	23	24	0.043(9)	0.028(4)	$^{+0.04}_{-0.013}$
	25	17	0.023(5)		
2	15	65	0.010(3)	0.0101(14)	$^{+0.003}_{-0.0016}$
	37	57	0.0100(16)		
3	22	89.7	0.010(4)	0.006(2)	±0.0002
	29	87.7	0.005(2)		
4	18	93.9	0.009(2)	0.0083(10)	±0.0002
	50	93.8	0.0082(12)		
5	2.139×10^5	95.6	100	100	...
	6.182×10^5	95.4	100		...
9	3.986×10^4	100	17.81(10)	17.85(5)	±0.3
	1.157×10^5	100	17.86(6)		

two runs, we obtain 714(4) keV and 847(5) keV in excellent agreement with the literature values, 713.2(14) keV and 846(2) keV.

2. Relative intensities

The determination of the intensities of the low-energy α lines relative to the most intense α line is presented in Table I. The number of coincidence events observed, N, with the α particle detected in DSSSD 3 and the ^{16}O ion detected in DSSSD 2, is given in the second column. The coincidence-detection efficiency, ε, determined from Monte Carlo simulations and arbitrarily fixed to 100% for line 9, is given in the third column. The efficiency-corrected intensity, I, relative to that of line 5, is given in the fourth column, and the average of the two runs is given in the fifth column. Finally, the systematic uncertainty on the intensity is given in the last column. The results of the two runs are generally in good agreement. Note the large systematic uncertainty on line 1.

For lines 1 and 2, the systematic uncertainty is dominated by the uncertainty on the ADC cutoffs and the dead layer thickness. For lines 3–5 and 9, the systematic uncertainty is dominated by uncertainties in the modeling of the ^{16}O ions as they strike the aluminum grid that covers 4–5% of the detector surface.

TABLE II: Overview of the rare decay sequences inferred from the observation of the new low-energy lines.

Line	Decay sequence	b_β (%)	Γ_γ/Γ (%)
1	$^{20}\mathrm{Ne}(5.621) \xrightarrow{\alpha} {}^{16}\mathrm{O}_{\mathrm{gs}}$	< 0.007	...
	$^{20}\mathrm{Ne}(9.873) \xrightarrow{\gamma} {}^{20}\mathrm{Ne}(5.621) \xrightarrow{\alpha} {}^{16}\mathrm{O}_{\mathrm{gs}}$	0.028(14)[a]	≈ 7[a]
	$^{20}\mathrm{Ne}(10.274) \xrightarrow{\gamma} {}^{20}\mathrm{Ne}(5.621) \xrightarrow{\alpha} {}^{16}\mathrm{O}_{\mathrm{gs}}$	2.877(42)[a]	0.084(17)[b]
2	$^{20}\mathrm{Ne}(5.788) \xrightarrow{\alpha} {}^{16}\mathrm{O}_{\mathrm{gs}}$	0.0016(5)	...
3	$^{20}\mathrm{Ne}(12.39) \xrightarrow{\alpha} {}^{16}\mathrm{O}(6.130) \xrightarrow{\gamma} {}^{16}\mathrm{O}_{\mathrm{gs}}$	0.0010(3)[c]	...
4	$^{20}\mathrm{Ne}(10.274) \xrightarrow{\gamma} {}^{20}\mathrm{Ne}(6.725) \xrightarrow{\alpha} {}^{16}\mathrm{O}_{\mathrm{gs}}$	2.877(42)[a]	0.046(6)[d]
	$^{20}\mathrm{Ne}(11.262) \xrightarrow{\gamma} {}^{20}\mathrm{Ne}(6.725) \xrightarrow{\alpha} {}^{16}\mathrm{O}_{\mathrm{gs}}$	0.205(26)[a]	6.5(8)[d]

[a] Value from Ref. [13]

[b] Using $\Gamma_\gamma = 0.097(14)$ eV [15] and $\Gamma = 116(17)$ eV determined in the present work.

[c] The ratio of the phase space available for β decay and electron-capture decay (EC) to the 12 390 keV state suggests that this would be a 'mixed' transition with $\mathrm{EC}/\beta = 0.16$.

[d] Branching ratio inferred under the assumption that the decay sequence accounts for all the observed events.

3. Origin of the low-energy lines

For easier reference, our suggested decay sequences are summarized in Table II. The detailed arguments are as follows.

a. Lines 1 and 2. The energies of the two lowest-lying α lines are consistent with α decay of the 3^-, $T = 0$ state at 5 621 keV and the 1^-, $T = 0$ state at 5 788 keV to the ground state of ^{16}O. The intensities are consistent with first-forbidden β transitions. However, it is possible that allowed β transitions to higher lying states followed by γ decay to the 5 621 keV and 5 788 keV states also contribute. In fact, the IAS is known to decay to the 5 621 keV state with a partial γ width of $\Gamma_{\gamma_1} = 0.097(14)$ eV [15]. The α width of the IAS has been determined to be $\Gamma_\alpha = 116(20)$ eV [16]. It follows that $\Gamma_{\gamma_1}/\Gamma_\alpha = 8.4(19) \times 10^{-4}$. In comparison, the efficiency-corrected relative intensity determined from the present data is $I_1/I_9 = 1.6(2)^{+2.2}_{-0.7} \times 10^{-3}$, implying that decays through the IAS account for approximately 20–100% of the observed intensity of α line 1; the wide range reflects the large uncertainty on the efficiency correction. Furthermore the 3^+ state at 9 870 keV is known [3] to be fed in β-decay with a branching ratio 0.028(14) and to γ-decay to the 5 621 keV state with a branching ratio about 0.07 [13], thereby giving a contribution of roughly the same magnitude as decays through the IAS. Note that the efficiency correction assumes a first-forbidden β transition to the 5 621 keV state. However, since the combined recoil caused by a β transition to the IAS followed by a γ transition to the 5 621 keV state is similar in magnitude, the two decay modes should have similar efficiency corrections. We note that γ transitions to the 5 788 keV state have not been observed [15].

b. Line 3. The third α line is located at $E_\alpha = 1\,220(30)$ keV, which corresponds to an excitation energy of 6 260(40) keV in ^{20}Ne, assuming that the α decay proceeds to the ground state of ^{16}O. No state is known in ^{20}Ne at this energy. In fact, the observed width of line 3 is incompatible with such a hypothesis: Assuming a reduced α width equal to the Wigner limit [17], one obtains an s-wave α width of only 7.9 keV due to the small relative energy.[1] Since no other particle-decay channels are open, this represents an upper limit on the total width of the state. However, the observed width of line 3 is 150(30) keV, well above the estimated experimental resolution of ≈ 35 keV. Converting the energy scale from α-energy to excitation energy, this corresponds to a width of $\Gamma = 190(40)$ keV, well above the Wigner limit.

β particles were detected in the 1.5 mm thick silicon detectors placed behind the DSSSDs. The ratio of triple coincidences ($\beta + \alpha + {}^{16}$O) to double coincidences (α+^{16}O) is shown in Fig. 4. This 'β ratio' displays a clear systematic dependence on α energy except for line 3, which has a very small β ratio, consistent with zero at the 2σ level. This behaviour is suggestive of electron capture (EC). We have identified one possible decay sequence: The 1^+, 13 308 keV state in ^{20}Ne is only fed in EC decay. It α decays to the $3^-/2^+/1^-$ states in ^{16}O (cf. Fig. 9) with partial widths of 700/19/190 in units of eV, emitting α particles with energies of 1 960/1 330/1 170 in units of keV. The main α line at 1 960 keV would be buried under the tails of higher-lying α lines. However, the observed intensity of line 3 implies a $\log ft$ value of 2.3, an extremely unlikely possibility. We have searched for other potential candidates among the known states in ^{20}Ne, but have failed to find any. The origin of line 3 thus remains mysterious.

We note, however, that the sd-shell model calculations of Ref. [18] predict both a 3^+ state at 11 400 keV and a 1^+ state at 12 200 keV to be populated in β decay. None of these states have been observed in β decay yet, but β decay to the 1^+ state with the calculated strength followed by α decay to the 3^- state in ^{16}O would explain the properties of line 3, provided the 1^+ state lies at the slightly higher energy of 12 390 keV. At this elevated energy β decay will still be favored over EC decay with a phase-space ratio of EC/$\beta = 0.16$. It would thus appear that the proposed decay sequence is inconsistent with the anomalous low β ratio of line 3. However, the parameter driving the systematic behavior seen in Fig. 4 is the β energy, not the α energy. In the proposed decay sequence the β energy is much smaller than the α energy would indicate because the decay feeds an *excited* state in ^{16}O; if the decay were to feed the ground state the α energy would be 6 130 keV. Indeed, the β ratio of line 3 is in good agreement with the observed systematics at 6 130 keV.

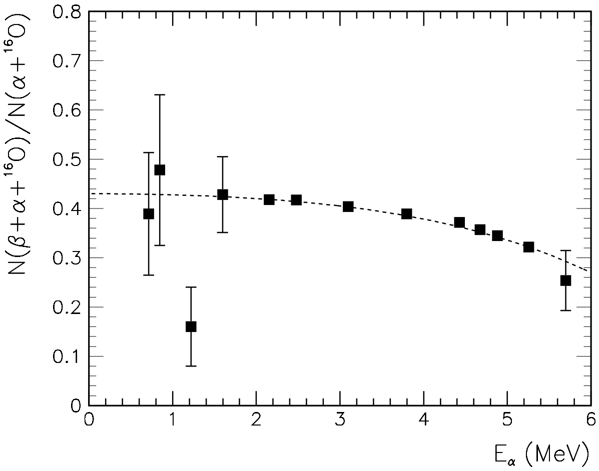

FIG. 4: Ratio of triple coincidences ($\beta + \alpha + {}^{16}$O) to double coincidences (α+^{16}O). The dashed curve is only meant to guide the eye. The error bars show the statistical uncertainty.

We note that the α threshold in ^{16}O is only 1 MeV above the 3^- state and that, in principle, population of unbound states in ^{16}O is possible in the decay of ^{20}Na. We have searched for such β-delayed two-α events, but found no significant signal above background.

c. Line 4. In Ref. [3] it was suggested that line 4 should be attributed to the α decay of the 0^+, $T = 0$ state in ^{20}Ne at 6 725(5) keV. The excitation energy deduced from the present data is 6 716(6) keV, thus supporting this interpretation. The intensity is a factor of two below the intensity obtained in Ref. [3]. We are unable to account for this discrepancy. As argued in Ref. [3], the direct population of a 0^+ state requires a second-forbidden transition, which results in a much smaller intensity than the intensity actually measured. Two alternative explanations were offered: (i) a β branch feeding a hypothetical state at 12 758 keV, which α decays to the 0^+ first-excited state in ^{16}O at 6 049 keV, and (ii) a weak β branch feeding a hypothetical state around 11 000 keV in ^{20}Ne, which decays mainly by γ-ray emission to the 6 725 keV state. It was already noted in Ref. [3] that alternative (i) is unlikely to be the correct explanation because the β branch would have a very small $\log ft$ value of 3.28. We can fully rule out alternative (i): Since the 6 049 keV state in ^{16}O decays by e^+e^- emission, the β ratio should be significantly higher (roughly a factor of 3) for α line 4 compared to all other α lines. Fig. 4 clearly shows that this is not the case. We cannot confirm nor rule out alternative (ii). Instead, we offer a third and fourth alternative: (iii) a weak γ branch from the IAS to the 6 725 keV state and (iv) a weak γ branch from the 1^+, $T = 1$ state at 11 262.3(19) keV to the 6 725 keV state.

We first consider alternative (iii): Based on the observed intensities, we can easily estimate the width of the proposed γ branch,

---

[1] This calculation assumes a 'standard' channel radius of $a = 1.4\ \text{fm} \times (4^{1/3} + 16^{1/3}) = 5.8$ fm.

$$\Gamma_{\gamma_4} = \Gamma_\alpha \frac{I_4}{I_9} = 0.054(11) \text{ eV} , \quad (1)$$

where I_4 and I_9 are the efficiency-corrected relative intensities given in Table I and $\Gamma_\alpha = 116(20)$ eV is the α width of the IAS [16]. The least intense γ branch observed by Fifield *et al.* was that to the 4 967 keV with a partial width of 0.060(8) eV [15]. It is difficult to judge from their Fig. 2 whether a 0.054(11) eV branch to the 6 725 keV state could have gone unnoticed, but it appears possible, especially taking into account that the 6 725 keV state is fairly wide ($\Gamma = 19.0(9)$ keV).

Next, we consider alternative (iv): The 11 262 keV state is fed with a β-branching ratio of $b_\beta(11.262) = 0.205(26)\%$ corresponding to a $\log ft$ value of 3.72 [3]. α decay from the 11 262 keV state is parity forbidden[2] so it almost exclusively decays by γ emission. It is known to decay to the ground state and the first-excited state with relative intensities of 84(5)% and 16(5)%, respectively [20], and the partial width to the ground state has been determined to be 11(2) eV [21]. Based on the observed intensity of line 4, we can estimate the width of the proposed γ branch to be

$$\Gamma_{\gamma_4} = I_4 \Gamma_\gamma \frac{b_\beta(7.421)}{b_\beta(11.262)} = 0.086 \text{ eV} , \quad (2)$$

where I_4 is the efficiency-corrected relative intensity given in Table I, $\Gamma_\gamma = 13.3(2)$ eV is the total width of the 11 262 keV state and $b_\beta(7.421) = 15.96(22)\%$ is the β-branching ratio to the 7 421 keV state. The deduced width corresponds to an M1 transition strength of 0.043 W.u., which is a reasonable value. Furthermore, the branch is far smaller than the two known branches, so it could easily have been missed in the study of Berg *et al.* [20]; unfortunately, their γ spectrum only extends down to 6 MeV.

B. Energies and relative intensities

The literature data on the energies and relative intensities of the β-delayed α lines of ^{20}Na are from Refs. [3, 4, 22–24]. In Table III, we compare the present data to that of Refs. [3, 23, 24]. The lines are numbered as in our spectrum and letters are used to denote lines quoted in other papers, but not seen by us (as argued below most of these are due to misinterpretations). Line D, seen by Ref. [23] but not by Ref. [3], was not seen in the present study despite the higher statistics. The present data on the energies of lines 4–13 is consistent with the previous data. The energies of the two most intense α lines (5 and 9) used for the energy calibration, differ from the previous energies by a few keV. This is due to the updated value for the $\alpha + {}^{16}$O threshold in ^{20}Ne [25].

The intensity of line 9 agrees with the intensity reported in Ref. [23] but is slightly larger than the intensity reported in Ref. [3]. An older study [4] gives 17.39(11)% in agreeement with Ref. [3].

Only the low-energy lines and the two most intense lines are included for the present data. The less intense lines at higher energy can be influenced in position as well as intensity by interference effects so we shall give our results below, when we discuss the *R*-matrix fit (Table IV).

C. *R*-Matrix Analysis

We turn now to a detailed analysis of the β-delayed α-spectrum above 2 MeV. This part of the spectrum contains several resonances as well as indications of interference effects at lower intensity levels. The *R*-matrix formalism provides a suitable framework to incorporate such effects in a fitting routine, but reliable results can only be extracted once the experimental response function is fully understood.

1. *R-matrix parametrization*

The *R*-matrix parametrization allows extraction of energy-, width- and β-strength parameters for the resonance levels in question. The parametrization offers at the same time a more proper interpretation of the excitation energy distribution compared to earlier studies. We use the same procedure as in Ref. [5]. The probability for β decay to the excitation energy E, followed by breakup into the channel c, is given by

$$\begin{aligned} w_c\left(E\right) = & C^2 f_\beta\left(E\right) P_c\left(E - E_{\text{thres}}\right) \\ & \times \sum_{x=F,GT} \left| \sum_{\lambda\mu} \widetilde{g}_{\lambda x} \widetilde{\gamma}_{\mu c} \widetilde{A}_{\lambda\mu} \right|^2 , \end{aligned} \quad (3)$$

where the alternative parametrization of the level matrix $A_{\lambda\mu}$ is used, as given in Eq. 33 of Ref. [26]. In Eq. (3) the boundary parameter B_c is automatically set equal to the shift function $S_c\left(E_\lambda\right)$ for all levels. This ensures that the fitted parameters for the energy, E_λ, the β strength, $\widetilde{g}_{\lambda x}$, and reduced α width, $\widetilde{\gamma}_{\lambda\mu}$, becomes the so-called observed ones [26]. The notation x =F, GT refers to Fermi and Gamow-Teller decays respectively, f_β is the integrated phasespace available to the leptons, C is a normalization constant and P_c is the penetration function with E_{thres} being the α-threshold energy. The number of counts as a function of E is then

$$N\left(E\right) = \frac{NT_{1/2}}{\ln 2} w_c\left(E\right) , \quad (4)$$

---

[2] The parity-forbidden α-decay width has been determined to be $42(20) \times 10^{-6}$ eV [19].

TABLE III: Comparison of present energies and relative intensities to previous data.

Line	E (keV)			I_4 (%)			
	Present	Ref. [3]	Ref. [23]	Present	Ref. [3]	Ref. [23]	Ref. [24]
1	714(4)	· · ·	~ 780[a]	$0.028(4)(^{+40}_{-13})$	· · ·	~ 1.4[a]	
2	847(5)	· · ·		$0.0101(14)(^{+30}_{-16})$	· · ·		
3	1220(30)	· · ·	· · ·	0.006(2)	· · ·	· · ·	
4	1 589(5)	1 580(40)	· · ·	0.0083(10)(2)	0.020(4)	· · ·	
5	2 153.2(10)[b]	2 150.4[b]	2 150.4[b]	100	100	100	100
6		2 479.6(21)	2 483.5(25)		3.7(4)	3.91(24)	3.7(3)
A		2 659(7)	2 756(5)		0.074(6)	0.072	
7		3 570(25)	3 325(13)		0.39(4)	0.052	
8		3 799(3)	3 803.0(25)		1.510(27)	1.55(5)	1.6(2)
9	4 433.8(15)[b]	4 432.2[b]	4 432.2[b]	17.85(5)(30)	17.31(9)	17.83(27)	16.3(3)
10		4 675(3)	4 674.6(21)		0.553(15)	0.478(24)	0.45(6)
11		4 885(3)	4 884.4(25)		1.09(3)	1.15(4)	0.91(8)
B		4 966(7)	4 930(6)		0.075(9)	0.128	
C		5 106(7)	5 222(47)		0.055(7)	0.044	
12		5 249(4)	5 253.5(23)		0.165(11)	0.130(9)	
13		5 698(6)	5 691(4)		0.010(2)	0.012(2)	
D	· · ·	· · ·	5 896(6)	· · ·	· · ·	0.002	

[a] The evidence presented in Ref. [23] for the observation of this α group is meager.

[b] Used for energy calibration.

where N is the total number of counts and $T_{1/2}$ is the half life of ^{20}Na [13].

The observed α widths are extracted as

$$\Gamma_\lambda^{\mathrm{o}} = \frac{\sum_c 2P_c \widetilde{\gamma}_{\lambda c}^2}{1 + \sum_c \widetilde{\gamma}_{\lambda c}^2 \frac{\mathrm{d}S}{\mathrm{d}E}|_{E=E_\lambda}}, \tag{5}$$

and the procedure for determining the β-decay matrix elements is similar to the one in Ref. [27]

$$\begin{aligned} B_{\lambda F} =& C^2 g_{\lambda F}^2 \frac{B}{\ln 2} \\ & \times \sum_c \int_0^Q P_c\left(E - E_{\mathrm{thres}}\right) \left| \sum_\mu \widetilde{\gamma}_{\mu c} \widetilde{A}_{\lambda\mu} \right|^2 \mathrm{d}E. \end{aligned} \tag{6}$$

Here $B = 6144.2(1.6)\,\mathrm{s}$ [28] and Q is the β-decay Q-value. For $B_{\lambda GT}$ a factor of $\frac{g_V^2}{g_A^2}$ enters in the denominator. When calculating absolute $B_{F/GT}$ values the known decay branch ($\mathrm{BR}_\alpha = 20.05 \pm 0.36$ [3]) to α unbound levels in ^{20}Ne is used. Integration of eq. (3) (without C^2) over the full energy spectrum then yields the normalisation constant

$$C = \left[\frac{\mathrm{BR}_\alpha \ln 2}{T_{1/2} \int_0^Q w\left(E\right) dE} \right]^{1/2}. \tag{7}$$

In our analysis only the exit channel populating ^{16}O in the ground state has been included. Levels 11, 12 and 13 are above the threshold for decay to exited states in ^{16}O. Their contribution to the reduced α-widths have been investigated by performing a two-channel fit including the first exited 0^+ state in ^{16}O at 6 049.4(1) keV. From this test their contribution was found to be no higher than $10^{-3}\sqrt{\mathrm{keV}}$ which justifies the single-channel analysis.

2. Recoil Broadening

If the $^{20}\mathrm{Ne}^* \to \alpha + {}^{16}\mathrm{O}$ breakup occurs at rest, the energies of the α particle and the ^{16}O ion are fixed by energy and momentum conservation. The available energy is shared as $E_{^{16}\mathrm{O}}/E_\alpha = m_\alpha/m_{^{16}\mathrm{O}} = 0.25$. If the breakup is preceeded by a β decay, however, the energies of the α particle and the ^{16}O ion are smeared out due to the recoil motion of the $^{20}\mathrm{Ne}^*$ nucleus. The recoil motion also causes a small systematic shift of the mean energies which, however, may be safely neglected here. For a pure Fermi transition, the resulting energy distribution can be approximated by [29],

$$\rho(x) = \begin{cases} \frac{5}{8T_{\max}}(1 - x^4) & , \ -1 \le x \le 1 \\ 0 & , \ |x| > 1 \end{cases} \tag{8}$$

while, for a pure Gamow-Teller transition and the spin sequence $2^+ \to 2^+ \to 0^+$,

$$\rho(x) = \begin{cases} \frac{15}{16T_{\max}}(1 - 2x^2 + x^4) & -1 \le x \le 1 \\ 0 & |x| > 1 \end{cases} \tag{9}$$

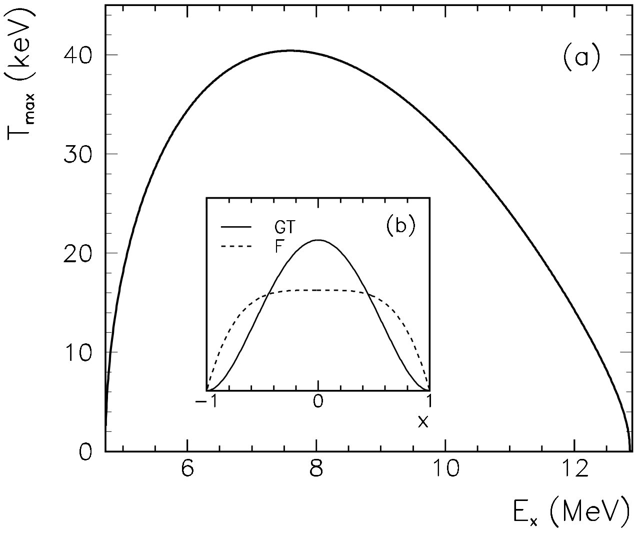

FIG. 5: Recoil broadening. (a) Maximum recoil shift as a function of the excitation energy in ^{20}Ne. (b) Fermi (F) and Gamow-Teller (GT) recoil broadening distributions.

with $x = \delta E / T_{\max}$ where $\delta E = E_\alpha - \langle E_\alpha \rangle$ is the shift relative to the mean α-particle energy and $T_{\max}$ is the maximum shift, given by

$$T_{\max} = \frac{m_e}{M} \left[2 Q m_\alpha c^2 (W_0^2 - 1) \frac{Mc^2 - m_\alpha c^2 - Q}{Mc^2 - Q} \right]^{1/2} , \tag{10}$$

where m_e, m_α, and M are the electron, α-particle, and ^{20}Ne masses; $Q = E_x - 4\,729.84$ keV and $W_0 = (E_0 - E_x)/m_e c^2$ where E_x is the excitation energy in ^{20}Ne and $E_0 = 13\,376$ keV is the maximum total β energy for decays to the ground state of ^{20}Na. In Fig. 5 (a) the maximum recoil shift, $T_{\max}$, is shown as a function of the excitation energy in ^{20}Ne, E_x. The inset (b) shows the different shapes of the recoil broadening distribution for Fermi (F) and Gamow-Teller (GT) transitions.

3. *Response Function*

The *response function* describes the distribution of energies measured from a perfectly monochromatic source due to experimental effects. We describe now how the response function is extracted from the experimental data.

The second most intense line (9) in the β-delayed α spectrum of ^{20}Na is found at $4\,434$ keV and results from transitions to the IAS in ^{20}Ne at $10\,273.2$ keV, the width of which is less than 0.3 keV [13]. The transition to the IAS is known [3] to be a mixed Fermi and Gamow-Teller type transition. However, the Gamow-Teller component is rather small so the broadening effect is well described by Eq. (8). Owing to the special structure and the $T = 1$ nature of the IAS, only little interference is expected with neighboring 2^+ states which could potentially distort the shape of the α line. The physical shape of the IAS α line is therefore well understood; this allows for a detailed study of the modification of the shape due to experimental effects.

We adopt a parameterization similar to the one used in Ref. [30] to describe the experimental response function. It consists of a Gaussian and a Gaussian folded through a low-energy exponential tail:

$$\begin{aligned} \psi(E_0, E) \; &= \; \frac{A_1}{\sqrt{2\pi}\sigma} \exp\left(\frac{(E - E_0)^2}{2\sigma^2} \right) \\ &+ \frac{A_2}{2\lambda} \exp\left(\frac{E - E_0}{\lambda} + \frac{\sigma^2}{2\lambda^2} \right) \times \operatorname{erfc}\left(\frac{E - E_0 + \sigma^2/\lambda}{\sqrt{2}\sigma} \right) . \end{aligned} \tag{11}$$

Here E_0 and E are the nominal and observed energies, λ the exponential decay "length" and erfc the complement of the incomplete error function. The normalization constants are $A_1 = 1/(1 + r)$ and $A_2 = r/(1 + r)$ where r gives the relative size of the second term compared with the first one. We find $\lambda = 25.5$ keV and $r = 0.085$. In addition we allow for contributions from low energy tails of higher lying Gamow-Teller fed resonances.

Ions striking the aluminum grid covering $g = 4.9\%$ of the detector surface experience additional energy loss compared to other ions, thus giving rise to a satellite peak at slightly lower energy. (The fit parameters are fairly strongly correlated so that almost equivalent fits can be obtained with different sets of parameters; we quote here a consistent set corresponding to the fit optimum.) The satellite is wider than the main peak due to the larger variation in effective thickness with angle. The final complete response function therefore reads:

$$\begin{aligned} \Psi(E_0, E) \; &= (1 - g)\, \psi(\sigma; E_0, E) \\ &+ \; g\, \psi(\sigma_g; E_0 - E_g, E) , \end{aligned} \tag{12}$$

where E_g is the mean energy loss in the grid, $\sigma = 10.2$ keV the Gaussian width of the main peak and $\sigma_s = 25.2$ keV the Gaussian width of the satellite peak.

The shape of the IAS α line, including experimental effects, is found by convolution of the response function, Eq. (12), with the recoil broadening distribution, Eq. (8), i.e.

$$\frac{\mathrm{d}N}{\mathrm{d}E} \; = \int \Psi(E_\alpha, E)\, \rho(x(E_\alpha))\, \mathrm{d}E_\alpha \, . \tag{13}$$

Fig. 6 shows the line shape measured in DSSSD 1 with the recoil broadening distribution, the response function, and the best fit using Eq. (13) superimposed.

The response function, $\Psi(E_0, E)$, is hereby obtained at $4\,434$ keV. In order to determine the response function for a general α-particle energy, we (1) assume that the exponential tails are independent of energy; (2) convert the energy loss in the aluminum grid, E_g, into an equivalent thickness (0.60 μm) which we use to calculate the energy loss in the grid for other α-particle energies; and finally (3) assume the Gaussian width of the satellite peak, σ_s, to be proportional to E_g.

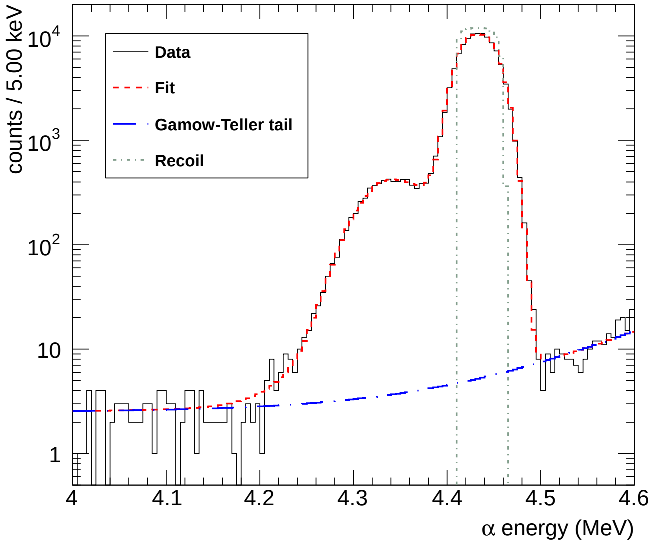

FIG. 6: (Color online) Singles spectrum between 4 and 4.6 MeV measured in DSSSD 1. The short-dash-dotted (green) curve shows the recoil broadening distribution, Eq. (8). The long-dash-dotted (blue) line shows the contribution from GT transitions to the low-energy tails of higher-lying states, modeled as an exponential function. The dashed (red) curve shows the best fit to the data using Eq. (13).

4. *Synthesis and Fitting*

The ft values obtained in Ref. [3] suggest that the transitions to the observed resonances are first forbidden or allowed, and hence the spin-parity could be 1^-, 2^+ or 3^-. (The observation of α decay from these states excludes unnatural spin-parity.) We shall attempt first the simplest possible fit based exclusively on allowed transitions to resonances seen earlier in reaction experiments. All resonances will then have spin-parity 2^+ and interference occurs naturally.

The delayed particle spectrum recorded in DSSSD1 during the second ^{20}Na run has been fitted using the maximum likelihood estimator [31] for the excitation-energy region 7.00–12.00 MeV. Figure 7 displays both the fitted R-matrix function (eq. 4) and the final fit curve obtained after convolution with the response function and the recoil broadening distribution. The deviation between the data and the fit is largest at the satellite shoulder of the most intense peak and dominates the rather high $\chi^2/\mathrm{d.o.f.} = 2.21$. This deviation is caused by systematic errors in the propagation of the response function to other energies. The inability of the fit to describe the few events around 9.8 MeV is due to inaccurate modeling of the low-energy response tail of the IAS. The fit results are listed and compared to literature values in Table IV.

As starting point in the fitting procedure the fairly well known level energies were fixed whereas the more uncertain reduced α-widths and some β-strength parameters were left free. Eventually all parameters were varied except for the IAS reduced α-width, γ_9, which in the literature has the upper limit $\Gamma_{\mathrm{tot}} \leq 0.3\,\mathrm{keV}$. Due to lack of sensitivity to such a small width γ_9 was kept at $-6.09 \times 10^{-3}\sqrt{\mathrm{MeV}}$ corresponding to $\Gamma_{\mathrm{tot}} = 0.200\,\mathrm{keV}$ throughout the minimization. To reproduce the data it was necessary to include a broad level at 8 767(23) keV; we shall comment on this below.

The uncertainties on the R-matrix parameters $\sigma(E_\lambda)$, $\sigma(\gamma_\lambda)$ and $\sigma\left(g_{\lambda,\mathrm{F/GT}}\right)$ were calculated by adding their individual errors in quadrature. The error originating from the response function was estimated by comparing fits using two different response functions: One that includes the low energy tail of the IAS and one that does not. The detailed error budget is as follows.

Energy parameters (E_λ): Errors on E_λ from the energy calibration range from 1.4 keV to 3.0 keV while the statistical fit errors range from 2×10^{-3} keV to 4.5 keV. The response function errors on E_λ are in general small but relatively large for levels 7 and 13.

Reduced width parameters (γ_λ): The response errors dominate since the reduced widths are highly sensitive to the detector response. The errors are around $2\text{-}4 \times 10^{-3}\sqrt{\mathrm{keV}}$ for all levels except level 7 for which it is $2 \times 10^{-2}\sqrt{\mathrm{keV}}$. The statistical errors are at the $10^{-3}\sqrt{\mathrm{keV}}$ level. The uncertainty on $\Gamma_{\mathrm{tot},\lambda}$ is found directly by combining $\sigma(\gamma_\lambda)$ and eq. (5).

β-strength parameters ($\mathbf{g}_{\lambda,\mathbf{G/FT}}$): The statistical errors dominate giving contributions around 10^{-3} for all levels apart from levels 6, 12 and 13 where they are one order of magnitude larger. The uncertainty on $\mathrm{B}_{\mathrm{F/GT}}$ is obtained through propagation of errors in eq. (6) where $\sigma(\mathrm{BR}_\alpha)$ is the dominating source of uncertainty.

5. *Discussion*

Our observed level parameters in Table IV will now be discussed and compared to the most recent ^{20}Ne evaluation [13]. Compared to earlier work we propose a new interpretation of the β-delayed α-spectrum from ^{20}Na.

The energy positions of levels 5, 9, 10, 11, 12 and 13 found in this work are in agreement with the literature values within one standard deviation. Levels 6, 7 and 8 differ slightly more, we note that their energy region contains clear interference effects.

The literature widths in Table IV are total widths, many are quite uncertain so that a quantitative comparison to our values is not possible. For levels 5, 7, 8, 10, 11 and 12 our widths are more precise than the literature ones. The width of level 5 differs significantly from the one in [13] but agrees well with a newer value of 9.0(13) keV [8]. In the case of level 6 the value of 180(80) eV is too small to be trusted and our poor determination for level 13 is attributed to the low level of statistics in this part of the experimental spectrum.

The calculated $B_{\mathrm{F/GT}}$ values are compared to those

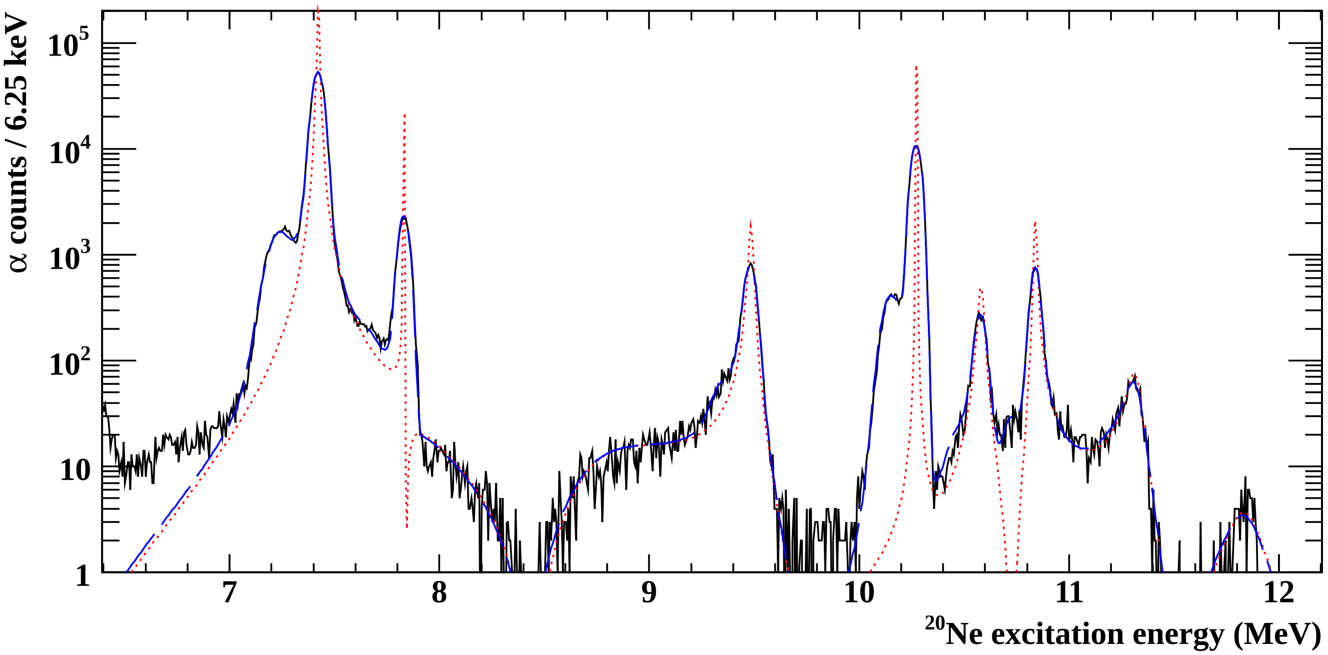

FIG. 7: Best fit to the experimental data. The graph shows the fitted R-matrix expression (eq. 4) (dashed), the convoluted expression (long-dashed) and the data (solid).

TABLE IV: Results expressed as observed R-matrix parameters E_λ, Γ_α and $B_{F/GT}$ with comparison to literature values.

	This work			Compilation [13]		Reference [3]
Level	E[MeV]	Γ_α[keV]	$B_{F/GT}$	E[MeV]	Γ_{total}[keV]	$B_{F/GT}$
5	7.4227(15)	10.0(5)	0.246(4)	7.4219(12)	15.1(7)	0.240(8)
6	7.8301(14)	0.18(8)[a]	0.017(7)	7.8334(15)	2	0.0126(5)
7	8.767(23)	686(56)	0.00230(7)	9.00(18)	800	0.008(12)[b]
8	9.4927(19)	35(3)	0.0329(8)	9.483(3)	29(15)	0.032(2)
9	10.274(2)	0.2	1.95(3)	10.2732(19)	≤ 0.300	2.06(6)
10	10.587(2)	34(2)	0.069(2)	10.584(5)	24	0.067(5)
11	10.842(2)	16.4(5)	0.258(5)	10.843(4)	13	0.224(15)
12	11.331(3)	85(6)	0.127(4)	11.320(9)	40(10)	0.101(14)
13	11.89(5)	252(70)	0.11(10)	11.885(7)	46	0.039(19)

[a] The systematic uncertainty is larger than the quoted fit uncertainty.

[b] In [3] the level is located at 9.196(30) MeV.

from Clifford *et al.*, which were obtained by conversion from the reported log ft values. Agreement within one standard deviation is only obtained for levels 5, 6, 8 and 10 albeit level 9 nearly agrees. The large difference for level 13 is again ascribed to the few events collected in that region while the disagreement for levels 7, 9, 11 and 12 largely has to do with our reinterpretation of the α-spectrum.

The analysis performed by Clifford *et al.* does not take interference effects into account. The events between level 11 and 12 in their interpretation therefore suggest the presence of two new levels in ^{20}Ne (level 10 and 11 in figure 4 in [3]), levels that have not been seen in other reactions. Our analysis, which treats interference effects properly, shows that constructive interference between levels 11 and 12 naturally reproduces the spectral shape in this region.

Clifford *et al.* explained the characteristic structure around 8 − 9 MeV by postulating the existence of two new levels in ^{20}Ne at 8 058 keV and 9 196 keV, but they do mention that interference between the 9 196 keV level and other levels could explain the 8–9 MeV structure. Our analysis does not include the 8 058 keV level (only reported by Clifford *et al.*). The interference effects are

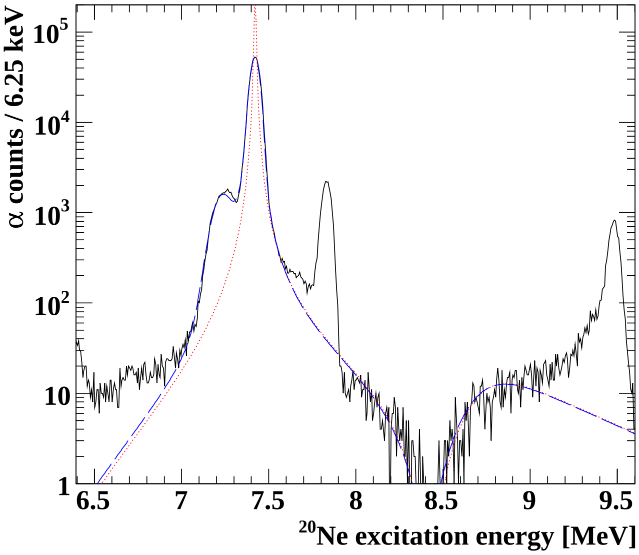

FIG. 8: The R-matrix expression (eq. 4) including only levels 5 and 7 plottet against data. This is **not** a fit, but the best-fit parameters for the two levels are used. Shown is the R-matrix expression (eq. 4) (dashed), the convoluted expression (long-dashed) and the data (solid).

here very important and are mainly due to destructive interference between level 5 and 7. This is shown explicitly in figure 8 where eq. (4) including only levels 5 and 7 is plotted.

Clifford *et al.* briefly mention the possibility that the 9 196 keV level identified by them could be identical to a known broad level at 8 800 keV. Indeed a level with 2^+ had been observed at $\approx 8\,800$ keV both in $^{16}\mathrm{O}(\alpha,\alpha)$ [32] and $^{19}\mathrm{F}\left(^3\mathrm{He,d}\right)$ [33] reaction experiments. Later Burlein *et al.* [34] measured the $^{20}\mathrm{Ne}(\pi,\pi')$ reactions, reported $\mathrm{E} = 9\,000(200)$ keV and $\Gamma = 800$ keV for this level and identified it as the 2^+ member of the 0^+_4 rotational band in ^{20}Ne. The present result, $\mathrm{E} = 8\,770(20)$ keV and $\Gamma = 686(56)$ keV, is the most precise observation of the 2^+_4 level and the first conclusive observation in β-decay.

The pronounced $^{16}\mathrm{O} + \alpha$ cluster structure of ^{20}Ne has been verified both experimentally [35-37] and theoretically [38] and several rotational bands containing resonances with very large α widths have been identified. The properties determined for the 8 770 keV resonance in our work clearly indicate cluster structure. Its large α-width points to a substantial overlap with the exit channel wave function indicating a large $^{16}\mathrm{O} + \alpha$ component. More quantitatively $\gamma_7^2 = 0.320$ MeV is close to the Wigner limit γ_w^2 of 0.344 MeV, evaluated with a radius of $r_0 = 1.5\left(16^{1/3} + 4^{1/3}\right)$ fm. The cluster structure is consistent with the small $\mathrm{B_{GT}}$ value determined in this work; an allowed Gamow-Teller transition to a pure ^{16}O + α cluster state would be Pauli blocked.

As a final remark we note that the position for level 7 agrees fairly well with the position found in a theoretical study [38] for the 2^+_4 state, thus supporting our assignment.

6. IAS properties

Our results give, when combined with earlier experiments, improved information on the IAS. First we consider the fraction of delayed α-particles coming from the IAS. This is best estimated from the singles spectrum, Fig. 2, by including the intensity above 1.5 MeV. This lower limit is varied by 100 keV to estimate the systematic uncertainty. The DSSSD detectors have a singles α particle efficiency that varies slightly with energy and has been determined in Ref.[5], the data are corrected for this effect. Each DSSSD gives an independent value for the ratio. The four values are consistent and lead to a final value of $I^\alpha_{IAS}/I^\alpha_{tot} = 0.1391(5)$. Compared to the previous value of 0.1386(33) [3] the precision is improved significantly.

Our second result is the total β-α strength for the IAS of 1.95(3) given in Table IV. The β-α strength is a product of the β strength and the branching to the α decay channel and must be corrected with the factor $\Gamma^{IAS}_\alpha/\Gamma^{IAS}_{tot}$. This factor can be estimated in the following way. The total Fermi strength is $2(1-\delta_c)$ where the correction factor according to theory [3] is 0.014(5). Combining this with the ratio of Gamow-Teller to Fermi strength, also measured in [3], gives a value for the total beta strength to the IAS that leads to $\Gamma^{IAS}_\alpha/\Gamma^{IAS}_{tot} = 0.92(3)$.

Alternatively, one may determine this ratio by measuring the γ-decays of the IAS. Several branches have been seen [15], the main one goes to the 1 630 keV level and constitute 88.9(5)% of all IAS γ-decays. (This number includes only observed transitions; as yet unobserved branches, such as the one to the 6 725 keV level discussed above, are not expected to change the value significantly.) Two relative intensities, that of the IAS transition to the 1 630 keV level relative to the total number of 1 630 keV γ-rays [39] and that of the total number of α-particles relative to the 1 630 keV γ-ray [3], now suffice to extract $\Gamma^{IAS}_\alpha/\Gamma^{IAS}_{tot} = 0.961(5)$, a value more precise than the above one.

Finally, one may include the measurements of α-radiative capture through the IAS to the 1 630 keV state [15, 16, 40], which give an average value of $5\Gamma^{IAS}_{\gamma\to 1.63}\Gamma^{IAS}_\alpha/\Gamma^{IAS}_{tot}$ of 19.5(1.5) eV [13], to put the relative measurements on an absolute scale. This gives a Γ^{IAS}_{tot} of 116(17) eV, which in hindsight justifies our use above of the 116(20) eV deduced in [16]. The difference to the value of 200 eV used in the fit (Table IV) will not affect the fit quality.

IV. SUMMARY AND CONCLUSION

The serendipitous improvements to the $\beta\alpha$ part of the decay scheme of ^{20}Na (see Fig. 9) presented here fall in two groups.

By measuring the α particle and the ^{16}O recoil ion in coincidence, we were able to identify three new β-delayed α groups below 1.5 MeV that, in the singles spectrum, are buried under the up to five orders of magnitude more intense ^{16}O recoil groups. The two lowest groups could be due to first forbidden transition (they arise from known negative parity states in ^{20}Ne), but at least the lowest one has an important contribution from $\beta\gamma\alpha$ decays through higher lying ^{20}Ne states. The origin of the third group is less certain, but it could be due to a combined EC-alpha-gamma and beta-alpha-gamma decay through excited states in ^{16}O. A fourth low-energy group is also due to $\beta\gamma\alpha$ decays.

The high level of statistics gathered in the present experiment allowed for an R-matrix analysis of the interference features seen in the β-delayed α spectrum around 3 MeV and 5 MeV. The spectrum turns out to be describable in terms of levels that all have been seen in reaction experiments. Compared to earlier β-decay studies we remove three suggested levels, but confirm conclusively β feeding to the broad state close to 9 MeV excitation energy in ^{20}Ne. The large width of this state suggests a pronounced $\alpha + {}^{16}$O cluster structure; our analysis gives improved values for its energy and width.

Most remaining questions on the ^{20}Na decay are minor and involve γ-decay. A dedicated study where α-γ coincidences were recorded may clarify the situation concerning the observed new low-energy α groups. Also of interest could be a search for population of unbound states in ^{16}O by detections of two-alpha events with a setup similar to the one used in the present work.

Acknowledgments

This work has been supported by the EU 6th Framework programme "Integrating Infrastructure Initiative - Transnational Access", Contract Number: 506065 (EURONS, JRA TRAPSPEC), by the Academy of Finland under the Finnish Centre of Excellence Programme 2006-2011 (Project No. 213503, Nuclear and Accelerator Based Physics Programme at JYFL), by the Nordic Infrastructure Project (NordForsk Project No. 070315) and by the Spanish Funding Agency MICINN on the project FPA2009-07387 O.S.K. acknowledges the support from the Villum Kahn Rasmussen Foundation, and A.S. acknowledges the support from the Jenny and Antti Wihuri Foundation.

---

[1] M. Wang, G. Audi, A. H. Wapstra, F. G. Kondev, M. MacCormick, X. Xu, and B. Pfeiffer, Chin. Phys. C **36**, 1603 (2012).

[2] R. D. MacFarlane, N. S. Oakey, and R. J. Nickles, Phys. Lett. B **34**, 133 (1971).

[3] E. T. H. Clifford *et al.*, Nucl. Phys. A **493**, 293 (1989).

[4] D. F. Torgerson, K. Wien, Y. Fares, N. S. Oakey, R. D. MacFarlane, and W. A. Lanford, Phys. Rev. C **8**, 161 (1973).

[5] O.S. Kirsebom et al., Phys. Rev. C **83**, 065802 (2011).

[6] S. Hyldegaard et al., Phys. Rev. C **81**, 024303 (2010).

[7] U. Hager et al., Phys. Rev. C **84**, 022801 (2011).

[8] H. Costantini et al., Phys. Rev. C **82**, 035802 (2010).

[9] J. Äystö, Nucl. Phys. A **693**, 477 (2001).

[10] J. Huikari et al., Nucl. Inst. Methods B **222**, 632 (2004).

[11] O.S. Kirsebom et al., Eur. Phys. J. A **47**, 1 (2011).

[12] O. Tengblad *et al.*, Nucl. Instr. Meth. A **525** 458 (2004).

[13] D. R. Tilley, C. M. Cheves, J. H. Kelley, S. Raman and H. R. Weller, Nucl. Phys. A, **636**, 249 (1998).

[14] J.F. Ziegler, J.P. Biersack, and M.D. Ziegler, *SRIM - The Stopping and Range of Ions in Matter*, 5th ed. (SRIM Co., USA, 2008)

[15] L. Fifield et al., Nucl. Phys. A **288**, 57 (1977).

[16] P. Ingalls, Nucl. Phys. A **265**, 93 (1976).

[17] T. Teichmann and E.P. Wigner, Phys. Rev. **87**, 123 (1952).

[18] B.A. Brown and B.H. Wildenthal, Atomic Data and Nuclear Data Tables **33**, 347 (1985).

[19] L. Fifield et al., Nucl. Phys. A **394**, 1 (1983).

[20] U.E.P. Berg et al., Phys. Rev. C **27**, 2981 (1983).

[21] W.L. Bendel et al., Phys. Rev. C **3**, 1821 (1971).

[22] J. Honkanen, Thesis, University of Jyväskylä Research Report 17, 1981.

[23] W. Huang *et al.*, Science in China A **40**, 638 (1997).

[24] S. Hyldegaard et al., Phys. Rev. C **80**, 044304 (2009).

[25] G. Audi, O. Bersillon, J. Blachot and A.H. Wapstra, Nucl. Phys. A **729**, 3 (2003).

[26] C. Brune, Nucl. Phys. A **718**, 472 (2003).

[27] F. Barker and E. Warburton, Nucl. Phys. A **487**, 269 (1988).

[28] I.S. Towner and J.C. Hardy, Rep. Prog. Phys. **73**, 046301 (2010).

[29] M. Bhattacharya and E. G. Adelberger, Phys. Rev. C **65**, 055502 (2002).

[30] M. Bhattacharya, E. G. Adelberger and H. E. Swanson, Phys. Rev. C **73**, 055802 (2006).

[31] S. Baker and R.D. Cousins, Nucl. Instr. Methods in Phys. Res. **221**, 437 (1984).

[32] L.C. McDermott, K.W. Jones, H. Smotrich, and R.E. Benenson, Phys. Rev. **118**, 175 (1960).

[33] H.T. Fortune, R.R. Betts and R. Middleton, Phys. Lett. B **62**, 287 (1976).

[34] M. Burlein et al., Phys. Rev. C **40**, 785 (1989).

[35] M.M. Hindi, J.H. Thomas, D.C. Radford, and P.D. Parker, Phys. Rev. C **27**, 2902 (1983).

[36] F. Michel, G. Reidemeister, and S. Ohkubo, Phys. Rev. C **35**, 1961 (1987).

[37] H.T. Richards, Phys. Rev. C **29**, 276 (1984).

[38] M. Kimura, Phys. Rev. C **69**, 044319 (2004).

[39] P. Ingalls, Phys. Rev. C **14**, 254 (1976).

[40] D.J. Steck, Phys. Rev. C **17**, 1034 (1978).

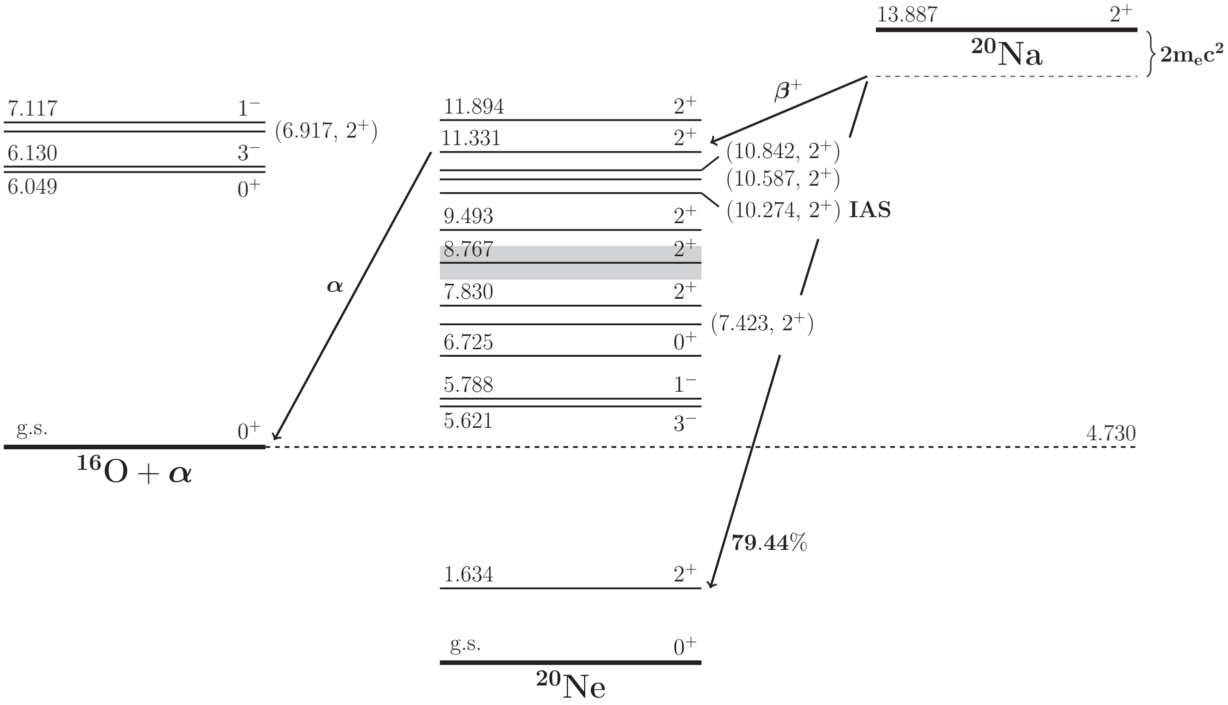

FIG. 9: Decay scheme for ^{20}Na. Details of several rare decays are given in Table II. Gamma rays in ^{20}Ne are not marked.